Identification of a Potential Geothermal Resource at Aguas de Vichy Hot Springs, Colombia, Through Integrating Geoelectrical and Electromagnetic methods

Authors

Juan C. Mejía-Fragoso[a, *], José D. Sanabria-Gómez[a], Rocío Bernal-Olaya[b]

[a]Universidad Industrial de Santander, Colombia

[b]Universidad Nacional de Colombia, Colombia

[*]Corresponding author: camilomejia.geo@gmail.com

Abstract

The Aguas de Vichy thermal spring, identified by the Colombian Geological Service (SGC) and located in Santander, Colombia, represents a significant but underexplored geothermal resource. This study presents the first geophysical imaging of the system, integrating Electrical Resistivity Tomography (ERT), Induced Polarization (IP), and Time-Domain Electromagnetics (TDEM) to characterize its structure. Existing geochemical analyses reveal high salinity and elevated temperatures, indicative of energy potential and an advection-dominated thermal regime. The geological context is marked by north−south and northeast−southwest fault systems intersecting Cretaceous and Precambrian rocks, overlain by a Quaternary aquifer.

Four ERT profiles and two TDEM soundings were acquired to characterize the geothermal system at Aguas de Vichy. ERT 1 and 2, crossing the main fault, revealed strong lateral resistivity contrasts (near 0 to > 1500 Ω·m) associated with clays, groundwater, and thermal anomalies, while the third ERT, located away from the fault, showed a predominantly resistive background suggesting limited geothermal influence. Complementary TDEM soundings extended the investigation to ~100m depth, identifying a low-resistivity anomaly interpreted as a geothermal reservoir and suggesting a fault-aligned hot-water plume feeding

the aquifer.

These findings support a convective flow driven by vertical fluid ascent along the fault zone in addition to the previous advection-based hypothesis. The integrated geophysical dataset highlights the complexity and geothermal potential of the system, providing critical insights for future exploration and contributing to Colombia's energy transition roadmap.

1 Introduction

Geothermal systems are commonly classified based on reservoir temperature into high (>180 °C), medium (100–180 °C), and low (<100 °C) enthalpy categories (Pesce and Miranda, 2003). While high-enthalpy systems are generally linked to active volcanic zones and used for power generation, low- and medium-enthalpy systems can also support thermal applications and electricity production through binary cycle technologies (Chandrasekharam and Bundschuh, 2008). Additionally, geothermal systems are categorized as convection- or conduction-dominated: convection-dominated systems involve heat transfer via fluid circulation driven by temperature gradients, often forming buoyant hydrothermal cells around heat sources (Yan et al., 2023; Redouane et al., 2022), whereas conduction-dominated systems rely on gradual heat diffusion through rock (International Geothermal Association (IGA), 2014). A subtype of convection-dominated systems are advective systems, where heat is transported by lateral or upward fluid flow along fault-permeable pathways driven mainly by hydraulic gradients rather than buoyancy (Hochstein et al., 2013; Christiansen et al., 2024).

A functioning geothermal system typically comprises four essential elements: (1) a heat source, which may be magmatic, mantle-derived, or related to deep crustal processes; (2) a permeable geological structure that controls the migration pathway of heat and fluids, such as faults, fractures, or porous layers; (3) a reservoir or storage unit capable of holding thermal fluids, often consisting of permeable sedimentary or volcanic formations; and (4) sufficient potential for economic recovery of the heat, either through direct use or electricity generation (International Geothermal Association (IGA), 2014). Geophysical methods are instrumental in detecting and delineating these components and enabling the development of conceptual models of the geothermal system.

Resistivity-based geophysical methods such as Electrical Resistivity Tomography (ERT) and Vertical Electrical Sounding (VES) have played a central role in characterizing geothermal systems since the mid-20th century (Zohdy et al., 1974). These techniques are sensitive to subsurface temperature, fluids, and structures, and are often integrated with other methods like

magnetotellurics (MT) and seismic imaging to build accurate geothermal models (Kana et al., 2015; Spichak and Manzella, 2009).

Globally, convection-dominated systems have been widely studied. In Hammam Sayala, Tunisia, ERT was used to construct a 2D geothermal model (Chabaane et al., 2017). In Langfang, China, a multi-method approach revealed geothermal fluid pathways and fault structures (Tian et al., 2022). Studies in Mexico's Los Humeros and Acoculco (Romo-Jones et al., 2021), Iceland's Krafla field (Arnason et al., 2000), and New Zealand's Wairakei-Tauhara (Hunt et al., 2009) further highlight the global emphasis on understanding convective heat transport.

In contrast, conduction-dominated systems, often located in sedimentary basins, are gaining attention through innovative applications. These include reusing abandoned hydrocarbon wells in China (Bu et al., 2012) and exploring onshore geothermal potential in Uruguay (Morales et al., 2021). In Colombia, the Llanos Basin has become a key focus. An operational example is Parex Resources' project in Campo La Rumba (Casanare), which utilizes high-temperature water co-produced during oil extraction to generate 35 kW, supplying 117 households El Nuevo Oriente (2024). Ecopetrol's pilot project in Chichimene (Meta) is designed for 2 MW generation, enough for over 6,000 homes (Jorquera, 2021). These initiatives reflect the growing interest in leveraging conduction-dominated geothermal resources in oil-producing regions (López-Ramos et al., 2022). Colombia's geothermal exploration dates back to 1968, beginning with ENEL's studies in the Nevado del Ruiz volcanic complex (Bona and Coviello, 2016). Later, the Colombian Geological Service (SGC) and other entities expanded efforts to regions such as Tufiño–Chiles–Cerro Negro (Mejía et al., 2014; Salazar et al., 2017). Most identified geothermal prospects are convection-dominated (Alfaro et al., 2020), including areas like Paipa (González-Idárraga, 2020) and Azufral (Murcia, 2020).

Initial estimates placed Colombia's hydrothermal potential between 700 and 1370 MWe (Gawell et al., 1999), increasing up to 2210 MWe with improved drilling and permeability techniques. By 2020, the SGC estimated 1170 MWe from only convective systems with surface manifesta- tions (Alfaro et al., 2020). Santander alone contributes 210 kWe to this estimate, with 80 kWe linked to the Aguas de Vichy hot springs, initially classified as advection-dominated (Alfaro, 2017) and significantly influenced by deep infiltration from a saline source, featuring saline waters at 100 °C (Alfaro et al., 2020).

In this study, we present the first geophysical imaging of the Aguas de Vichy geothermal system. Using resistive methods, we investigate subsurface conditions to delineate the distribution of geothermal fluids in the shallow aquifer, to test the hypothesis of this being a

convective geothermal system associated with a major fault. Understanding these dynamics will delineate the geological features to consider for a proper geothermal play definition.

2 *Aguas de Vichy* Thermal Springs

The municipality of San Andrés is situated at 6°49'N latitude and 72°51'W longitude, at an altitude of 1,617 meters above sea level. The region has an average temperature of 19°C and is located 104 kilometers away from Bucaramanga. The municipality covers an area of 278 km². Within the municipality, a thermal spring emerges along the banks of the Guaca River, three kilometers south of the town center via the road to Molagavita and Málaga. To reach the spring, one must walk approximately 500 meters west from the road to the river channel. This thermal spring is named *Aguas de Vichy* (Alfaro and Ortiz, 2011) (Figure 1).

The area is notably affected by intense faulting and folding, predominantly oriented N-S and NE-SW. A covered fault at the spring emergence point, mapped with a NNW-SSE orientation, juxtaposes Paleozoic units with Cretaceous units (Ward et al., 1977). Another structural feature, the Baraya fault, is located two kilometers east of the spring. This N-S trending normal fault with right-lateral movement juxtaposes sedimentary rocks from the Paleozoic, Jurassic, and Cretaceous periods.

The geological units outcropping range from the Ordovician (pre-Devonian) to the Quaternary. Generally, there are intrusive igneous rocks from the Jurassic (Santa Barbara quartz monzonite) that intrude older metamorphic rocks such as the Bucaramanga Gneiss and the Silgará Formation, which constitute the crystalline basement of the area. Above the basement, a series of sedimentary units are deposited, ranging from the Devonian to the Quaternary. These sequences have different contact relationships with each other and are also affected by significant structural control, evidence of the complex geological history of the area (Figure 1).

The thermal waters in San Andrés are classified as sodium chloride type, enriched with notable levels of bicarbonates and calcium (Table 1). Taking into account the elevated levels of total dissolved solids and the specific ionic composition, it is hypothesized that these waters are significantly influenced by deep infiltration from a saline source (Alfaro and Ortiz, 2011), dominated by an advection (Alfaro, 2017).
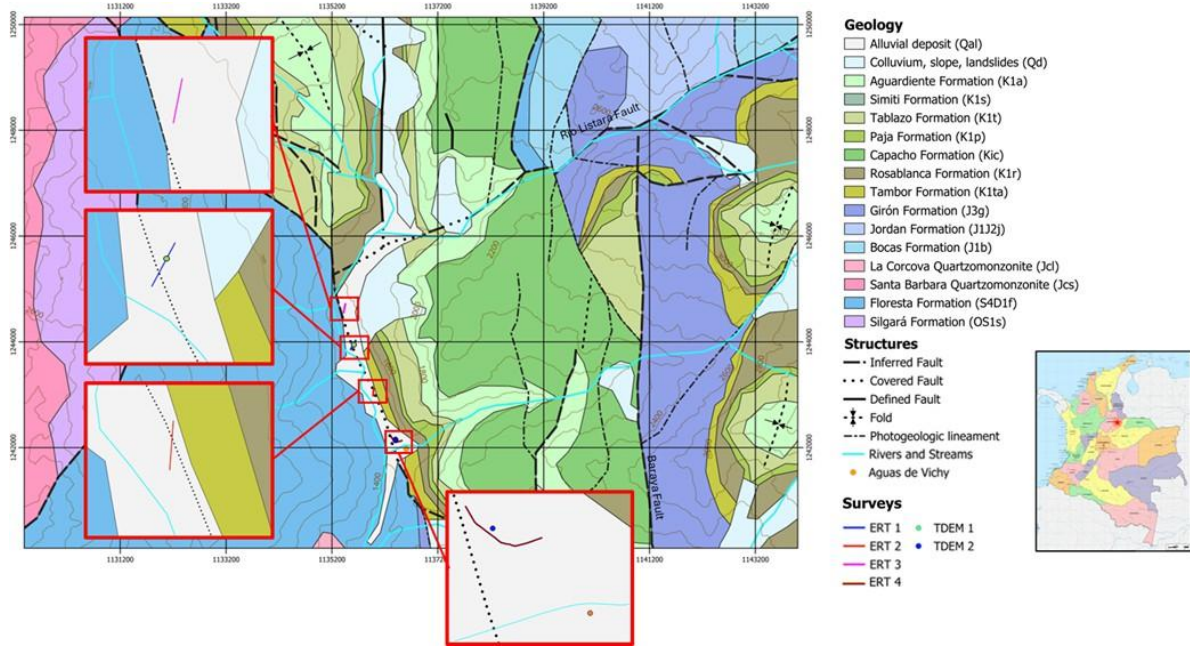
Figure 1: Location of the *Aguas de Vichy* thermal springs, geological map and location of the ERT surveys. Modified from (Ward et al., 1977) and (Alfaro and Ortiz, 2011).

The quaternary deposit was classified as an alluvial deposit (Alfaro and Ortiz, 2011), though it has not been extensively studied further. Alluvial deposits are typically found in ravines, streams, and broad topographic surfaces, often forming well-developed terraces, particularly along the margins of river valleys. They result from the transport and deposition of material by water. These deposits are composed of clays, sands, granules, pebbles, cobbles, and blocks with shapes that vary from angular to rounded; they may also exhibit complex lateral facies variations (Miall, 2014). The *Aguas de Vichy* thermal springs are probably influenced by multiple water sources, these may include geothermal fluids that rise through convection, meteoric waters, and surface waters from the river and streams that recharge the aquifer. Then, the water flow within the aquifer may be influenced by lateral connectivy and heterogeneity of the alluvial deposit, rather than solely by a saline or geothermal source.

Table 1: Geochemical values corresponding to *Aguas de Vichy* (Alfaro and Ortiz, 2011).

Code	Location Name	Total Alkalinity (mg CaCO3/L)	Total Dissolved Solids (mg/L)	Na	K	Mg	Ca	Mn	Fe
SAN001	Vichy Waters	720	360.2	58.5	20.2	218.5	6	0.08	0.42

Theoretical estimates for the geothermal reservoir associated with the Aguas de Vichy thermal springs suggest promising potential, based on a volumetric model by Alfaro et al. (2020). Assuming a reservoir temperature of 100 °C—classifying it as medium-enthalpy— and a surface temperature of 31 °C, the model yields a mean electric potential of 0.08 MWe, with a 90% confidence interval ranging from 0.03 to 0.13 MWe (Table 2). The simulation assumes a 30-year

5

project life and a recovery factor of 0.10. It is important to note that the model uses generalized assumptions—such as reservoir areas between 1 and 3 km², thicknesses from 1 to 2.5 km, and a uniform porosity of 0.11—without incorporating detailed geological data from the site. While the results are subject to considerable uncertainty, they highlight the potential viability of the system and justify further exploration.

Table 2: Estimated electric potential from volumetric model (Alfaro et al., 2020).

Parameter	Minimum	Expected	Maximum
Deposit area (km²)	1.0	2.0	3.0
Deposit thickness (km)	1.0	1.5	2.5
Reservoir temperature (°C)	31	100	100
Porosity	0.10	0.11	0.15
Recovery factor	0.05	0.10	0.25
Electric Potential (MWe)	Mean: 0.08 (90% CI: 0.03–0.13)		
Stored Heat Energy (EJ)	Mean: 0.61 (90% CI: 0.31–0.90)		

3 Method

To investigate the *Aguas de Vichy* geothermal system, we employed an integrated geophysical approach combining Electrical Resistivity Tomography (ERT), Induced Polarization (IP), and Transient Electromagnetic Soundings (TDEM). These methods were selected for their complementary sensitivity to subsurface properties relevant to geothermal exploration, including fluid salinity, temperature, clay content, and structural discontinuities.

ERT was used as the primary imaging tool, given its ability to resolve resistivity contrasts associated with thermal plumes, aquifer heterogeneity, and fault zones. Because temperature and salinity significantly affect subsurface conductivity (Hermans et al., 2012; Revil et al., 1998; McInnis et al., 2013), and electrical resistivity typically decreases with increasing temperature (Revil et al., 1998; Llera et al., 1990), saline thermal fluids are expected to exhibit lower resistivity than surrounding Quaternary deposits and fresher groundwater. ERT therefore provides an effective means to delineate geothermal fluid migration and identify plume pathways (Hermans et al., 2012). IP measurements were acquired along selected ERT profiles to enhance the discrimination of clay-rich confining units and improve the interpretation of fluid-saturated zones.

TDEM soundings were included to extend the depth of investigation beyond the limits of ERT, enabling the detection of deeper conductive anomalies potentially associated with a geothermal

reservoir. Together, these methods allow us to evaluate both the shallow aquifer and the deeper structures suspected to control heat and fluid transport.

The survey design consisted of several ERT-IP transects oriented across the inferred fault zone, with electrode arrays optimized to detect lateral and vertical resistivity variations. TDEM stations were positioned along and between ERT lines (Figure 1) to ensure spatial correlation and depth continuity. This configuration was chosen to test the hypothesis that the main fault acts as a vertical conduit facilitating the ascent of geothermal fluids from depth to the surface.

To support the field interpretation, we developed a synthetic resistivity model representing the expected geological framework. The model consisted of a low-to-medium resistivity aquifer overlying a fault zone, bringing into contact the high-resistivity Floresta Formation and the medium-to-high resistivity Tambor Formation. This conceptual model informed the inversion setup and provided a reference for interpreting anomalous zones in the field data.

3.1   Synthetic Model

The synthetic model was executed to understand how resistivity inversion would appear under the hypothesized subsurface conditions. PyGIMLi (Rücker et al., 2017), which offers comprehensive computational tools to simulate complex subsurface resistivities, was employed to this end. Initially, we established a 2D geometric model representing the Floresta formation, the Tambor formation, the aquifer/deposit, and the fault, assigning specific resistivity values to each. The resistivity values were estimated based on the studies of García-Arias et al. (García-Arias et al., 2024) and Saad et al. (Saad et al., 2012). We set up an electrical resistivity tomography (ERT) measurement scheme using 64 electrodes evenly spaced along a line extending from 0 to 170 units, and used a computational mesh to define the spatial domain. To model the injection of geothermal fluid into the aquifer, an injection point was established at the fault and the intersection of the quaternary deposit.

Here, we simulated the geothermal fluid as a diffusive substance with a peak concentration value of 100% at the injection point, applying a diffusion coefficient to represent the spread of the fluid. Boundary conditions included zero concentration (Dirichlet condition) at the external boundary and consistent fluid influx (Neumann condition) at the injection point.

After solving the diffusion equation, we refined the visualization by interpolating the concentration values to the mesh cell centers and reducing any negative concentration values

to zero to ensure physical precision. Considering the property of interest is resistivity, a linear inverse relationship between resistivity and concentration of the difussive fluid was established across the aquifer. This relationship ranged from a minimum to a maximum resistivity value, effectively linking concentration with the electrical properties of the geological medium: higher concentrations of the difussive fluid correspond to lower resistivity and vice versa (Figure 2a and 2b).
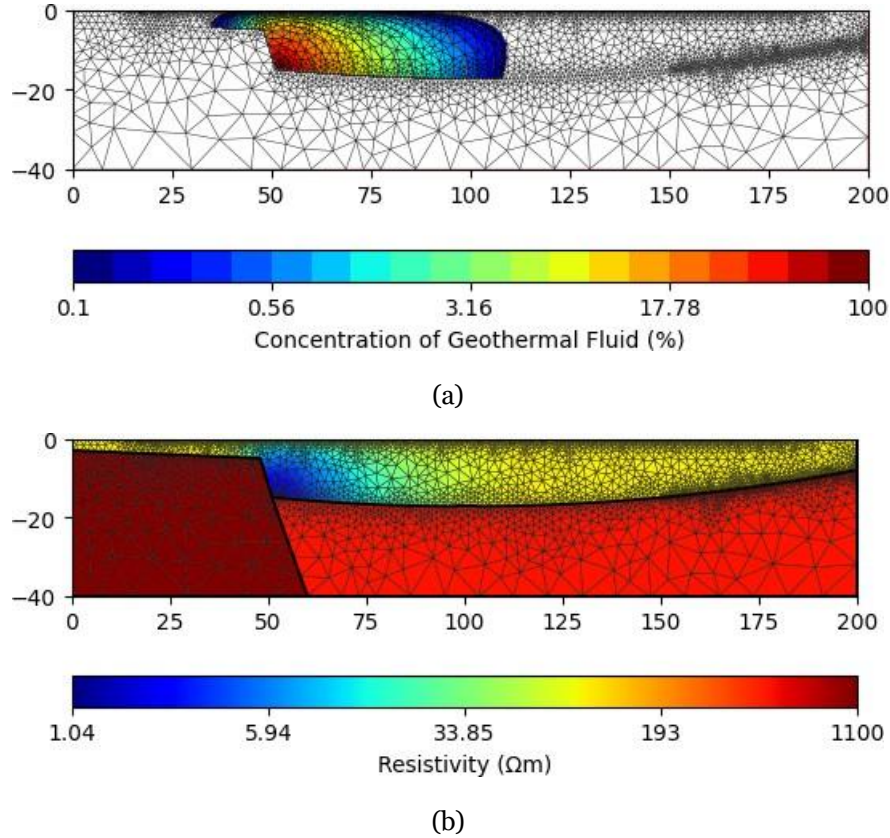

(a)

(b)

Figure 2: Overview of the subsurface modeling: (a) Structure of the isolated diffusive fluid (geothermal plume) as a function of its concentration, (b) Synthetic subsurface resistivity including the geothermal plume

Upon completion of the synthetic model, we proceeded to simulate the Electrical Resistivity Tomography (ERT) data, utilizing the calculated resistivity distribution as the model parameter.

To achieve the highest level of detail possible, we decided to use the multiple-gradient array for the simulation, because of its proven high resolution and robustness against noise, as substantiated by the findings of (Dahlin and Zhou, 2006). The efficacy of this array configuration lies in its rapid data acquisition and enhanced data density, essential for intricate subsurface delineation. Moreover, its ability to attenuate noise impacts renders it highly suitable for simulating realistic environmental conditions, thereby bolstering the

reliability of the data (Dahlin and Zhou, 2004). To mirror actual field scenarios, we introduced a noise level of 3% alongside an absolute noise factor of $1 \times 10{-6}$. For consistency and repeatability of the stochastic elements within the model, a fixed random seed (1337) was employed. The inversion of the simulated ERT data was executed using Res2Dinv software (Loke, 2010), and the results, presented in Figure 3, corroborate the detectability of the hypothetical geothermal plume as a discernible low resistivity anomaly. Additionally, these results delineate the fault through a pronounced resistivity gradient and define the aquifer's lower boundary with remarkable clarity.
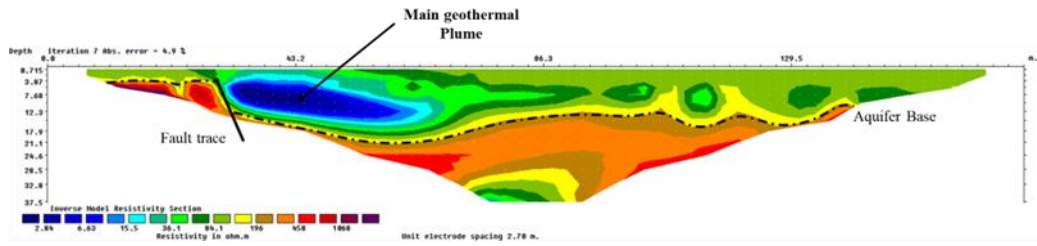

Figure 3: Inverted section of the synthetic model using Res2Dinv, the modelled geothermal plume can be seen as a low resistivity anomaly, while the fault appears as a high gradient of resistivity at the left.

3.2 Electrical Resistivity Tomographies and Induced Polarization

3.2.1 ERT and IP data acquisition

We employed the ZZ-Universal-96 acquisition system (ZZ Resistivity Imaging Ltd.) to conduct four Electrical Resistivity Tomography (ERT) surveys near the mapped fault zone. Three of these transects were acquired early in the campaign, with two complemented by Induced Polarization (IP) measurements to enhance subsurface discrimination. Given the fluvial-alluvial nature of the study area, known for its lateral facies variations (Miall, 2014), high-resolution imaging was essential.

To maximize data density, we used the proprietary ZZ array, which performs full-channel measurements: for every current injection (AB), the system records potentials at all remaining electrodes. This significantly improves resolution compared to conventional arrays. However, a small portion of the channels presented damage and were excluded from acquisition and inversion. ERT transects 1 and 2 intersected the fault zone on the alluvial terrace near the Guaca river, where the phreatic surface was expected to correlate with river elevation. ERT 3 was located within the Quaternary deposits, further from the fault, to evaluate the lateral continuity of the geothermal system. A fourth profile (ERT 4) was acquired near the Aguas de Vichy springs,

using a curved geometry adapted to the topography and a conventional Schlumberger array (Figures 1 and 4), helping to assess the resistivity distribution around the spring emergence and explore potential fluid continuity toward the southern margin. A summary of the ERT-IP acquisition parameters is provided in Table 3.

Table 3: Summary of the four ERT surveys, detailing parameters, settings, and geographic coordinates (MAGNA Bogotá). The orientation of all the surveys is SW-NE, and the ZZ array was used.

Survey	Channels	Spacing (m)	Length (m)	Unused electrodes	ERT	IP	Start Coordinate	End Coordinate	Array
ERT 1	64	3	189	37, 38, 40, 57, 58, 59	Yes	No	1243854.41 N, 1135560.46 E	1244020.64 N, 1135645.85 E	ZZ array
ERT 2	64	2.5	157.5	35, 37, 38, 40, 57, 58, 59, 63	Yes	Yes	1242977.403 N, 1135976.464 E	1243131.04 N, 1135988.524 E	ZZ array
ERT 3	32	5	155	N/A	Yes	Yes	1244553.70 N, 1135424.43 E	1244708.85 N, 1135453.98 E	ZZ array
ERT 4	32	7	217	N/A	Yes	Yes	1242210.81 N, 1136320.87 E	1242138.76 N, 1136496.20 E	Schlumberger

3.2.2 ERT and IP Preprocessing and Inversion

Following acquisition, a quality control phase was conducted to remove unreliable data based on the quality factor (Q), which quantifies the level of electrical noise. Data points with Q values above 30 were discarded, following manufacturer recommendations. Additional filters removed negative and extreme apparent resistivity values exceeding the 99th percentile. Data were formatted for inversion in Res2Dinv (Loke, 2010), and topography was incorporated via separate elevation files. IP data (ERT 2 and 3) followed the same preprocessing workflow.

Inversion parameters were chosen to balance model stability and flexibility. A damping factor of 0.15 (minimum 0.03) was used, with local optimization enabled to refine resistivity contrasts. The convergence criteria were set at 2.0% RMS change and 0.5% minimum line search change. Seven iterations were performed with robust data constraints (cutoff 0.05) and topographic correction via the FEM method. The extended model option was deactivated to avoid extrapolation beyond the electrode array.

Figure 5 shows the distribution of resistivity and chargeability data points across the model space. IP data had lower density but were concentrated in the upper portion of the array, consistent with expectations for shallow chargeable materials.
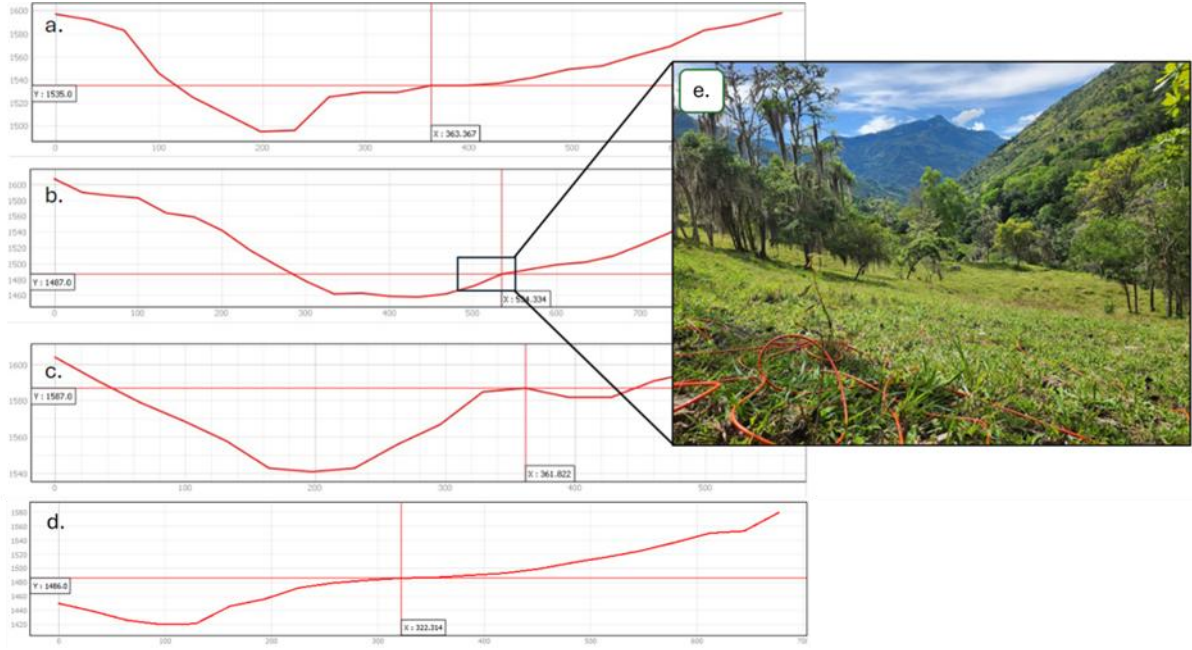
Figure 4: W-E topographic profiles for the ERT surveys, showing (a) ERT 1, (b) ERT 2, (c) ERT 3, and (d) ERT 4 locations, with an additional (c) detailed view of the ERT 2 study area.
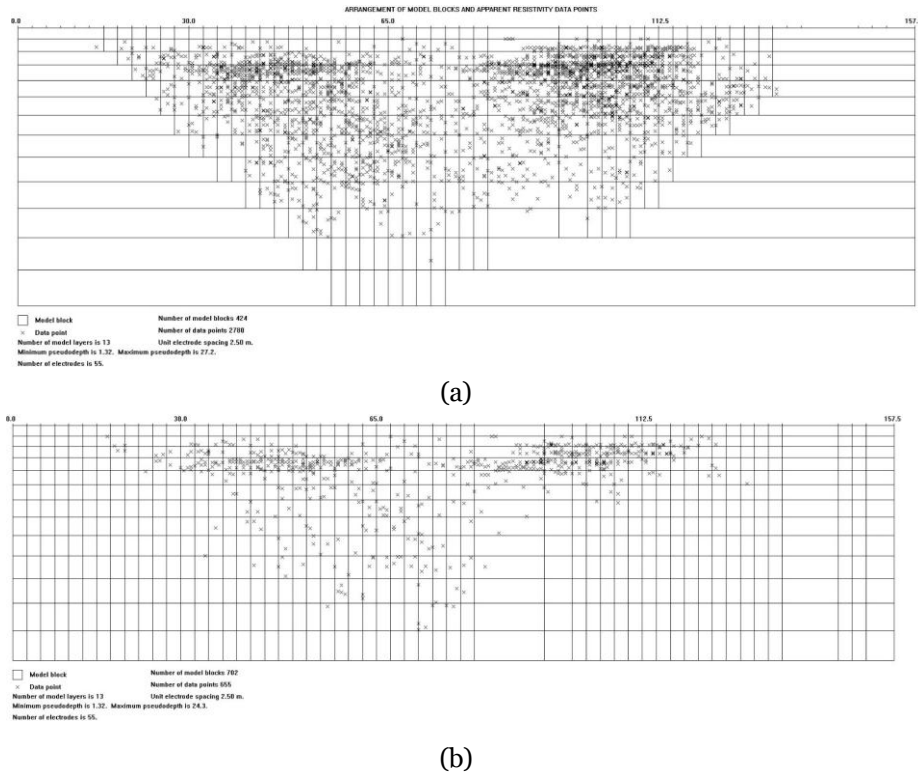

(a)

(b)

Figure 5: (a) Distribution of resistivity data points across ERT 2; (b) Chargeability data point density.

Post-inversion, error filtering was applied by excluding data points with errors exceeding 100%, and by iteratively removing outliers from the calculated vs. measured resistivity scatter plots. This process was repeated until achieving an optimal fit with minimal mean absolute error
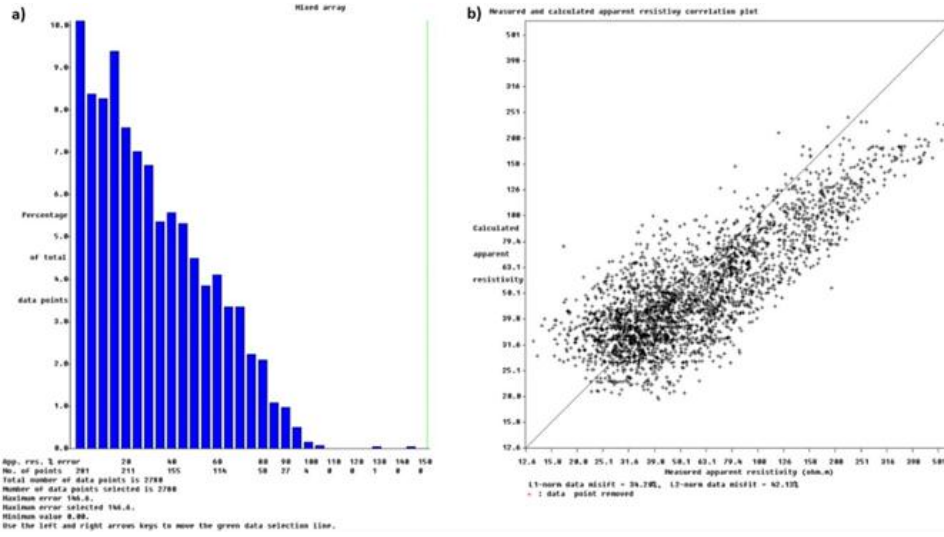
(MAE) variation (Figure 6).

Figure 6: Left: Histogram of error percentages for ERT 2; Right: Scatter plot of calculated vs. measured apparent resistivity after filtering.

3.3 Time-domain Electromagnetic Soundings (TDEM)

3.3.1 TDEM data acquisition

To extend the depth of investigation beyond the sensitivity limits of ERT, two 1D TDEM soundings were conducted at the locations of ERT 1 and ERT 4 (Figure 1). These soundings aimed to confirm the vertical continuity of low-resistivity anomalies and to identify deeper conductive features (>30 m) potentially associated with a geothermal reservoir. A square transmitter loop (40 × 40 m) was energized with a 12 V source, regulated by a resistor, and configured with a dual-moment setup (high: $700/5\,\mu s$, low: $125/3\,\mu s$). Measurements included 10 and 15 cycles, with 54 stacks and a repetition frequency of 240 Hz, with an average transmitted current of 1.02 A.

TDEM is particularly effective for imaging deep conductive structures, such as clay-rich layers or saline fluid accumulations, and is less sensitive to surface heterogeneities or electrode contact resistance. Integrating the TDEM results with ERT and IP profiles enhanced the structural and hydrogeological interpretation of the geothermal system.

3.3.2 TDEM Processing and Inversion

TDEM data were processed and inverted using Aarhus SPIA (Auken et al., 2015), which performs

1D laterally constrained inversion (LCI) based on a horizontally layered Earth assumption. The soundings were jointly inverted with spatial regularization to enhance lateral coherence across the profile. Inversion parameters incorporated instrument characteristics and topographic corrections.

The dataset used for inversion was acquired exclusively with the Small_Coil_RC-5 antenna, selected for its high resolution and sensitivity to conductivity variations within about 150 meters of depth. This configuration was particularly suited to delineating shallow-to-intermediate geothermal features and hydrogeological contrasts with enhanced vertical detail. Model evaluation focused on convergence stability, data misfit, and the depth of investigation.
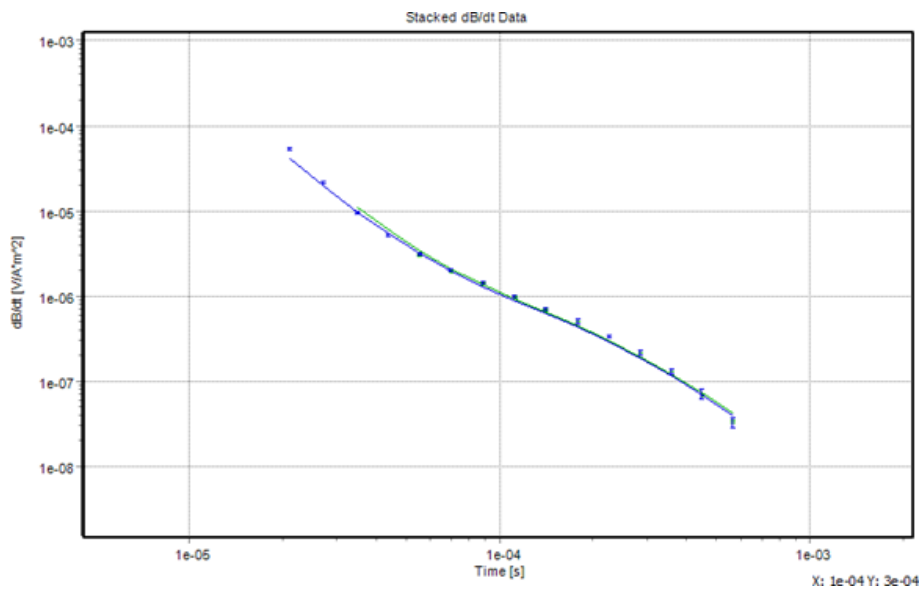

Figure 7: Log-log plot of measured vs. modeled dB/dt response for TDEM 1. Data residual: 2.07.

4   Results and Discussion

ERT and IP surveys were conducted on the aquifer associated with the *Aguas de Vichy* thermal springs. Through this process, we successfully generated five geo-electrical profiles of the subsurface, comprising three resistivity profiles and two chargeability profiles. Our results provide information on the physical properties of the subsurface. This allowed us to confirm the presence of the previously inferred fault, detect thermal water plumes associated with the fault and the base of the aquifer. To ensure visual consistency when comparing the results of the three ERT surveys, we standardized the color scale across all surveys using the same color scale. Specifically, the

13

lower limit of the color scale was set to match the lowest resistivity value observed among the three surveys. The interpretation of our results is based on direct and indirect measurements of subsurface materials from different authors (Table 4).

Table 4: Resistivity and Chargeability values for different materials.

Material	Resistivity (ohm.m)	Chargeability (msec)	References
Groundwater	$10 - 150$	< 1	(Telford et al., 1990), (Sabnavis and Patangay, 2006), (Akhtar et al., 2021)
Hot saline water	$0.2 - 5$	< 1	(Chabaane et al., 2017), (Hermans et al., 2012)
Clay	$5 - 160$	$15 - 90$	(McCarter, 1984), (Sill and Klein, 1981), (Suryadi et al., 2019)
Sand	$40 - 1500$	$2 - 12$	(Telford et al., 1990), (Abd Malik et al., 2022), (Sabnavis and Patangay, 2006)
Alluvium	$10 - 800$	$1 - 4$	(Telford et al., 1990), (Sabnavis and Patangay, 2006)
Sandstone	$8 - 4 \times 10^3$	$3 - 12$	(Telford et al., 1990), (Abd Malik et al., 2022), (Sabnavis and Patangay, 2006)

The ERT 1 resistivity profile (Figure 8) displays resistivity values ranging from $2.82 \; \Omega \cdot m$ to over $2000 \; \Omega \cdot m$. The lowest resistivities are interpreted as zones affected by thermal fluids, including both geothermal and mixed waters. It's important to note that this profile features a pronounced thermal water plume on its southwestern side, sharply delineated by a steep resistivity contrast, interpreted as a fault zone acting as a preferential conduit for geothermal fluid migration. This fault likely plays a dual role: as a structural control and a thermal driver, facilitating vertical ascent of deep fluids by convective mechanisms driven by density and temperature differences (Zongjun et al., 2014).

The ERT 1 profile closely resembles the synthetic model presented in Figure 3, particularly in the identification of a rising thermal plume and a fault that favors fluid migration. Granular patterns appear in both synthetic and ERT inversions. In the synthetic case, they can be attributed to meshing and regularization, given their simplicity and low contrast, while the field sections display higher-amplitude, spatially coherent and more complex contrasts, suggesting the presence of subsurface heterogeneity within the alluvial deposit of the study area.

This is consistent with the variability expected in fluvial settings (Miall, 2014) and with local descriptions of intercalated sand, gravel, and clay that produce zones of contrasting

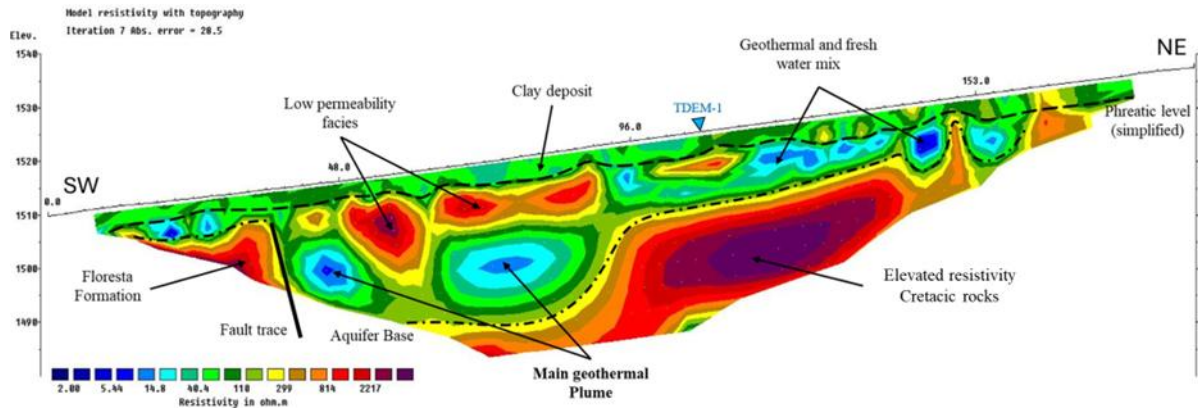permeability (Ríos et al., 2002).

Figure 8: Inverted resistivity profile for ERT 1, highlighting the fault trace, the main geothermal plume, the aquifer base, the TDEM-1 location and the lateral heterogeneity of the subsurface.

Such heterogeneity directly conditions the movement of the thermal plume. As a result, the fluvial depositional setting leads to an irregular distribution of thermal waters, unlike the more uniform behavior reproduced in the synthetic model. There is also a high-resistivity anomaly above the main geothermal plume, which may correspond to sandy, low-permeability facies acting as a cap or baffle. This feature likely influences the apparent resolution of the plume in the inverted resistivity sections by partially shielding or distorting its geometry.

The TDEM-1 sounding, located at the central portion of the ERT 1 profile, supports this interpretation by extending the depth of investigation beyond the ERT's 30 m range. The upper layers of the TDEM model (0–14.8 m) show resistivity values ranging from 22.9 to 101 $\Omega \cdot$ m, consistent with the resistivity values resolved in the ERT for that portion of the heterogeneous, alluvial deposit. Notably, the third layer (14.8–27.8 m, 149 $\Omega \cdot$ m) likely corresponds to the transition between the alluvial aquifer and the underlying Cretaceous bedrock, as suggested by both methods (Figure 9)

Below this contact, the TDEM model reveals a distinct low-resistivity zone (6.45 $\Omega \cdot$ m between 47–75 m depth), which is not resolved in the ERT profile. This deeper conductor is interpreted as a geothermal reservoir or zone of fluid accumulation, reinforcing the idea of vertical fluid migration through the fault and permeable zones, and subsequent lateral dispersion within the aquifer and stratigraphic permeable units in contact with the fault.

The phreatic level of the aquifer is inferred to be situated just above most of the low-resistivity zones associated with thermal water. This level aligns with the topographic elevation of the Guaca River, which is slightly above 1500 meters above sea level (MASL), as
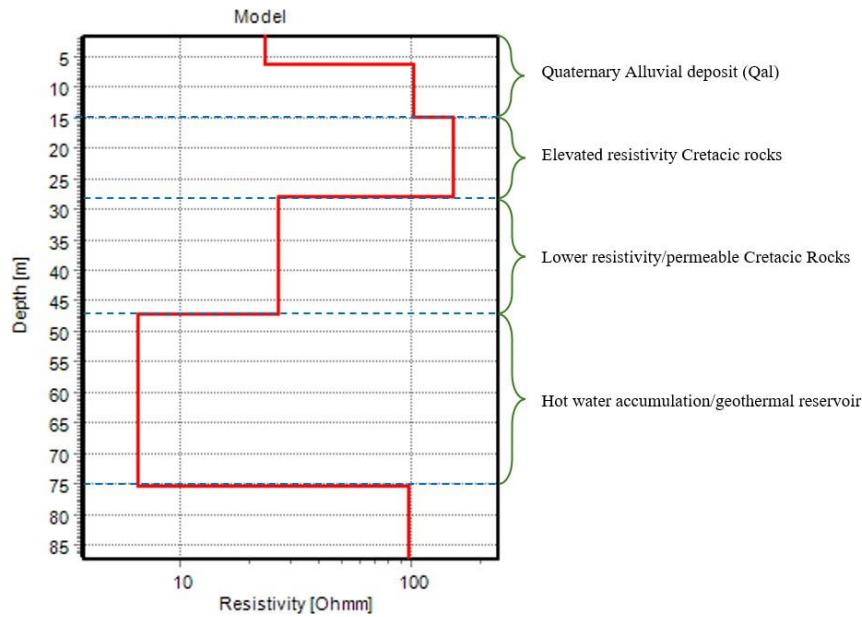
Figure 9: Inverted 1D resistivity model from TDEM-1 sounding, revealing the aquifer base and deeper conductive horizons interpreted as a geothermal reservoir, within a Cretaceous sedimentary context.

illustrated in Figure 4a. It is important to mention that the phreatic level may be more complex and irregular due to the complexity of the subsurface; however, we have provided a simplified representation. Above this phreatic level, zones of low to moderate resistivity are observed, suggesting the presence of a clay layer that may locally confine the aquifer, this clay layer may be laterally discontinuous as there are resistivity variations. The base of the aquifer, as well as the underlying Cretaceous rocks and the Floresta Formation, are also discernible in the resistivity profile.

Given that low resistivity anomalies are consistently distributed throughout the resistivity profile, it can be suggested that the aquifer, despite its lateral facies variations, has significant continuity. This continuity facilitates the movement of geothermal fluid through it, which indicates a lateral flow within the aquifer towards the thermal springs. The identified thermal plume suggest that the geothermal fluid not only moves laterally, but it ascend through the main fault due to heating in deep and convection.

The inverted resistivity section of ERT 2 (Figure 10a) reveals subsurface features consistent with those observed in ERT 1. The resistivity profile displays irregularly distributed, prominent low-resistivity zones throughout the aquifer, indicative of the presence of geothermal fluids, fresh water mix, and saturated clays. These zones are flanked by areas of higher resistivity, likely representing more consolidated or less saturated materials, which emphasize the lateral

16

facies variations characteristic of the aquifer. The profile also delineates a pronounced resistivity gradient towards the northeast (right side of the section), marking the fault trace. Adjacent to this fault, the main geothermal plume is visible, suggesting the fault's role as a primary conduit for thermal waters infiltrating the aquifer. Both the phreatic level and the aquifer base are visible within the section, alongside the Floresta Formation situated beneath the aquifer. A discontinuous clay layer at the top is also identified, potentially acting to locally confine the aquifer and, therefore, limiting its recharge through meteoric waters.
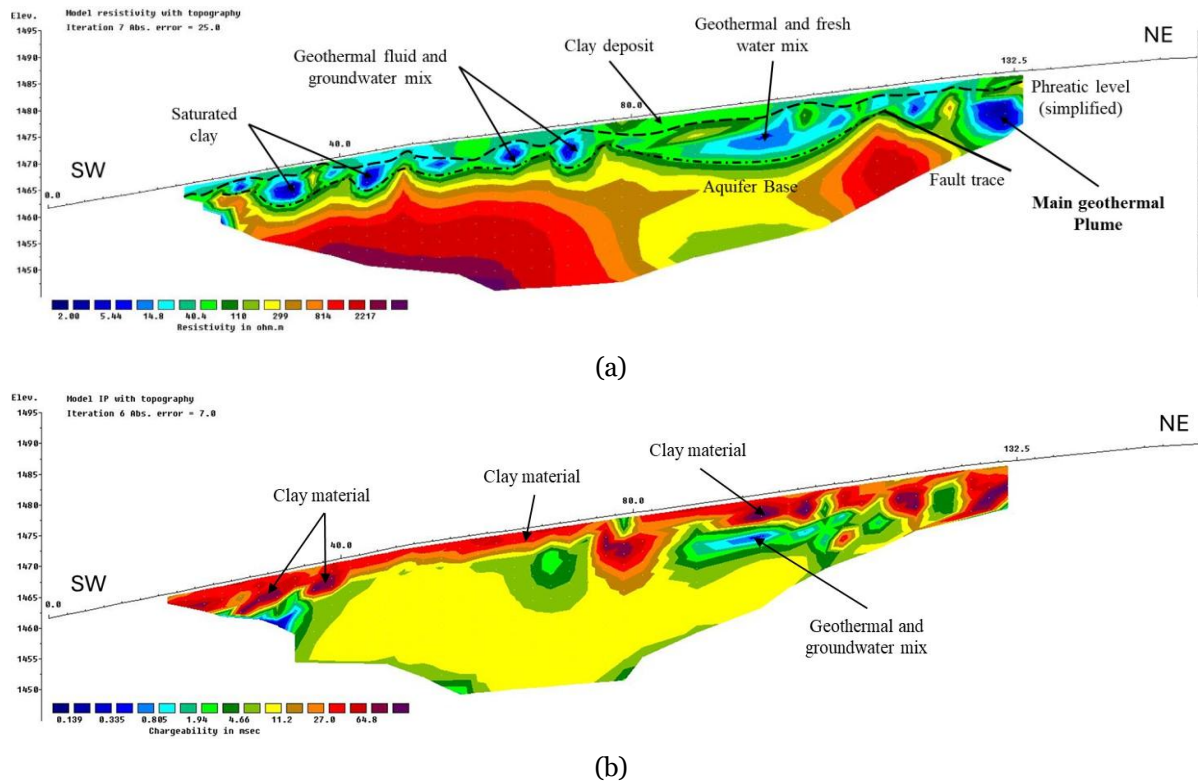

(a)

(b)

Figure 10: Inverted ERT 2 profiles, showing resistivity (a) and IP data (b). Key features include saturated clays, a clay layer, the main fault trace and the main geothermal plume identified.

Additionally, the IP profile acquired in the same transect of ERT 2 (Figure 10b), although offering less coverage deeper in the section and displaying most data points near the surface (as illustrated in Figure 5b), complements the resistivity data. It highlights regions of both low and high chargeability. The high chargeability at the top of the IP section is associated with polarizable materials such as clay, supporting the identification of this material within the deposit. Meanwhile, the low chargeability zones may validate the presence of geothermal fluids as they seem to be correlated with conductive zones, although less distinct than in the resistivity profile due to having fewer data and different resolution.

The geophysical signatures observed in ERT 1 and ERT 2 sections support the idea that

thermal waters are rising along the fault and spreading laterally within the aquifer, influenced by the complex interplay of geological facies and fluid dynamics. This dynamic not only suggests the presence of geothermal activity within the aquifer but also provides insights into the origin of the *Aguas de Vichy* thermal springs. The complex interaction between the convective flow of thermal waters through the fault and their dispersion through heterogeneous, permeable media enhances our understanding of the geothermal system and the aquifer's hydrogeological behavior, while also highlighting the broader challenge of elucidating fluid flow dynamics within heterogeneous reservoirs.

The inverted section of ERT 3 (Figure 11) differs significantly from the previous surveys by not crossing the fault and being located topographically further from the river compared to ERT 1 and ERT 2 (Figure 4). This section predominantly displays patterns consistent with a clay deposit rather than signs of geothermal activity. The resistivity profile (Figure 11a) exhibits higher resistivity values which might indicate less saturated zones, while localized lower resistivity areas suggest pockets of higher saturation or slightly different material composition, likely still within the predominantly clay deposit.
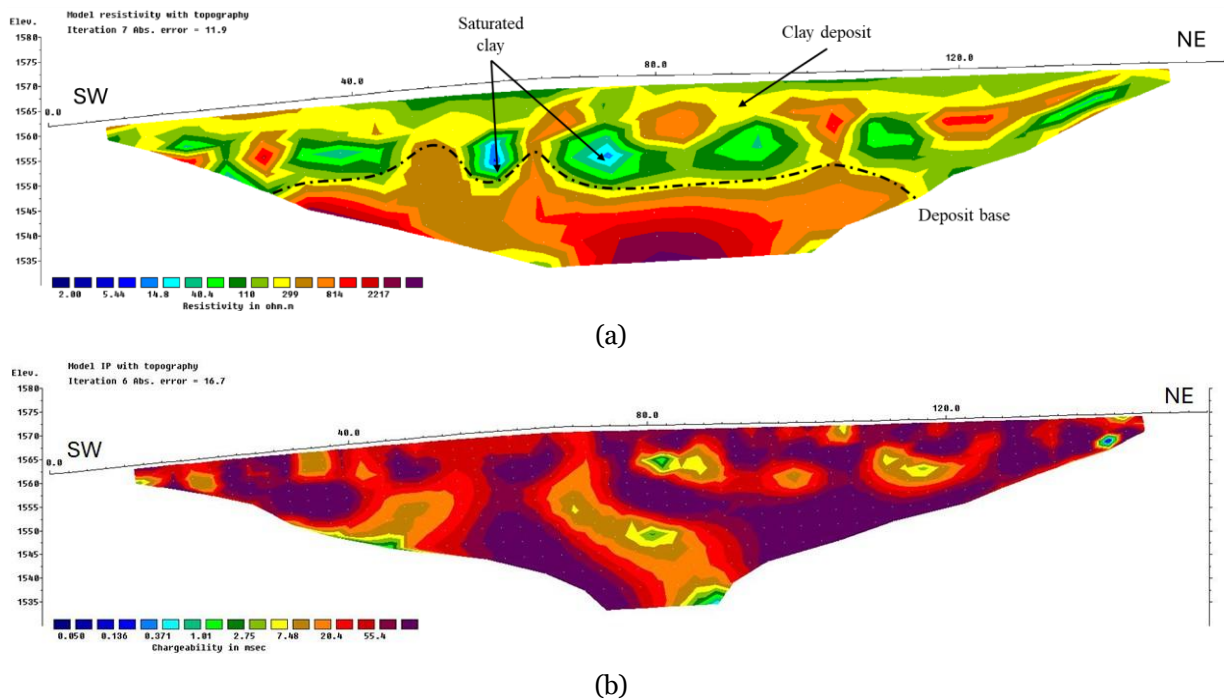

(a)

(b)

Figure 11: Inverted ERT 3 resistivity (a) and IP (b) profiles displaying subsurface features in the *Aguas de Vichy* area. Key elements include saturated clay layers and clay deposits, with a clear delineation of the deposit base.

The IP profile (Figure 11b) supports this interpretation by mostly showing areas of higher chargeability, which are typical of clay-rich formations due to their ability to polarize under

an electrical field. The absence of significant geothermal signatures and the relative consistency across the section suggest that this area of the deposit does not contribute to the geothermal dynamics and the fluid circulation observed in other sections.

Instead, it likely represents a more confined portion of the depositional system, less influenced by the river than the other profiles and the fault´s fluid flow, and characterized by higher clay content that may act as a hydraulic barrier within the aquifer. The results from ERT 3 support the interpretation that faulting plays a critical role in channeling and concentrating geothermal fluids, indicating the presence of a convective regime. However, the absence of a pronounced resistivity anomaly in this sector may reflect either a spatially limited extent of the fault-controlled flow or a reduced volume of geothermal fluid insufficient to sustain lateral migration at this distance.

The interpretation of ERT 4 reveals a stratified resistivity structure. A very resistive near-surface layer (depth < 5 m, resistivity > 1000 $\Omega \cdot$ m) is interpreted as dry soil or anthropogenic fill. Below this, a conductive zone (approximately 5–15 m depth) with resistivity values as low as 10 $\Omega \cdot$ m corresponds to a shallow aquifer, likely containing a mixture of geothermal and fresh water. This is followed by a moderately to high resistive layer (resistivity > 100 $\Omega \cdot$ m), extending to the base of the ERT profile (around 40 m), which is interpreted as colluvial or transitional material with reduced saturation or different lithology (Figure 12).
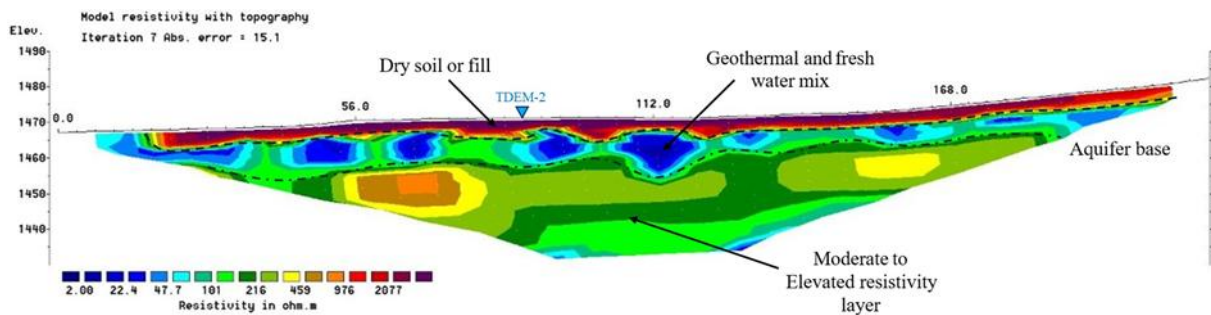

Figure 12: 2D resistivity model obtained from ERT line 4 using a Schlumberger array configuration; highlighting the different layers and the TDEM-2 location.

TDEM-2, located near the central portion of ERT 4, provides complementary insights by extending the depth of investigation beyond the ERT limits. The first TDEM layer (0–14.8 m) exhibits a relatively high resistivity of approximately 80 Ω·m, which appears inconsistent with the low-resistivity aquifer resolved in the ERT. This discrepancy is attributed to the limited vertical resolution of TDEM in shallow sections, where thin conductive features are averaged with more resistive materials above and below—particularly the dry superficial layer detected by the ERT.

Therefore, the first TDEM layer likely reflects an average response encompassing both the dry fill and the upper portion of the aquifer (Figure 13).
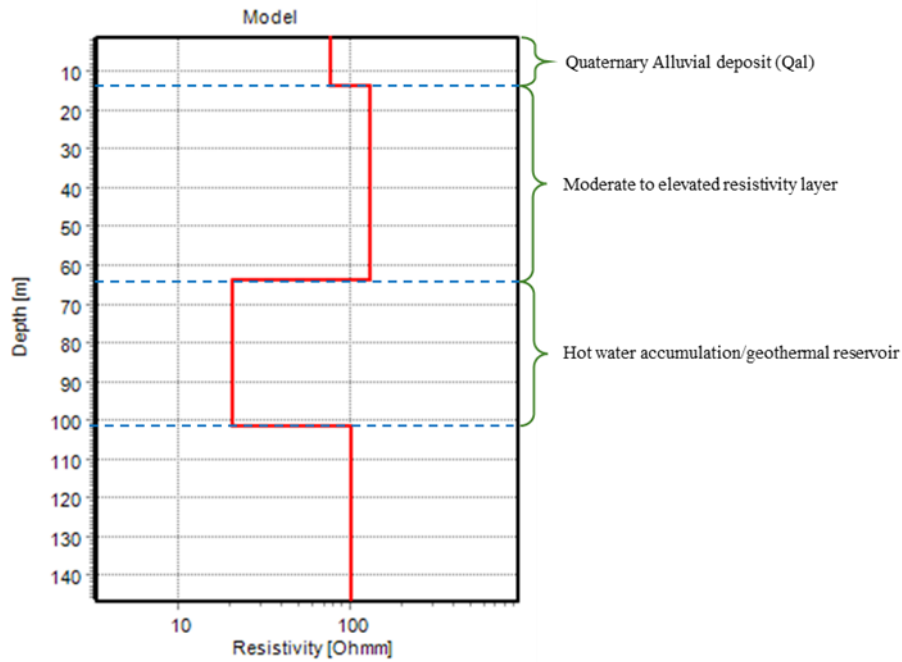

Figure 13: Inverted 1D esistivity model from TDEM-2 sounding, revealing the aquifer base and deeper conductive horizons interpreted as a geothermal reservoir, within a sedimentary context.

Beneath this, the second TDEM layer (14.8–63.5 m) exhibits elevated resistivity (120 $\Omega \cdot$ m), broadly matching the moderately resistive zone in the lower part of the ERT model. This layer may represent a transitional unit separating the shallow aquifer from deeper structures—possibly a colluvial deposit or compacted horizon. However, its precise nature remains unclear without lithological control, and further studies are needed to confirm its role in the hydrogeological system.

Importantly, the third TDEM layer (63.5–100.3 m) presents a marked decrease in resistivity (20 $\Omega \cdot$m), suggesting the presence of a deeper fluid-saturated zone not resolved by the ERT. This anomaly is interpreted as a geothermal reservoir or hot water accumulation, supporting the conceptual model of convective, vertical fluid migration through a fault, additional to the advective, deep reservoir connection Alfaro (2017) proposed. Below 100 m, resistivity increases again, possibly indicating the transition to more consolidated or less permeable bedrock.

Together, ERT 4 and TDEM-2 provide a coherent image of a shallow mixed aquifer system underlain by a deeper low-resistivity anomaly consistent with geothermal fluid accumulation. While the anomaly identified in ERT 4 differs from that observed in ERT 1 and 2, the combined results of TDEM-1 and TDEM-2 suggest possible lateral continuity of the geothermal system.

Despite the limited scope of detailed studies in the region, previous research by (Alfaro et al., 2020) has demonstrated substantial geothermal potential. The volumetric method and Monte Carlo simulations suggest a promising outlook for geothermal energy development, with expected electric potential capable of meeting regional energy demands (Table 2). Despite the promising geothermal potential and a viable reservoir temperature of 100°C, further exploration and detailed studies are necessary to more accurately assess the geothermal capabilities of the *Aguas de Vichy* springs, as the potential estimated for the thermal springs relies on standardized and generalized parameters rather than specific properties of the geothermal reservoir.

The apparent thermal gradient (ATG) estimated from the difference between reservoir temperature (100 °C) and spring discharge (31 °C) (Alfaro et al., 2020), divided by the depth of the conductive anomalies imaged by TDEM (47–100 m), yielded values between ~690 and 1470 °C/km. These numbers are one to two orders of magnitude higher than the regional conductive geothermal gradient reported for the study area (33–36 °C/km; (Mejía-Fragoso et al., 2024)) and exceed the maximum gradients measured in volcanic systems such as Las Nereidas (~140 °C/km; SGC data). Such values, however, should not be interpreted as true conductive geothermal gradients (Alfaro et al., 2009).

Instead, they should be regarded as a heuristic indicator of convective upflow, where the temperature drop occurs abruptly within the shallow aquifer and at the discharge zone. This behavior is consistent with international studies of high-enthalpy convective fields such as Wairakei–Tauhara (New Zealand), where reservoir intervals remain nearly isothermal and exhibit very low apparent gradients (<10 °C/km), following boiling-point-with-depth profiles rather than conductive trends (Scott et al., 2016; Farina et al., 2019; Qin et al., 2025). In this context, the extremely high ATG values at Aguas de Vichy are best interpreted as indicative of buoyancy-driven convection and rapid fluid ascent along the fault zone, rather than as conductive geothermal gradients comparable to regional maps.

Future work should aim to investigate the heat source responsible for the thermal characteristics of the waters, exploring in detail deeper geological structures that could be influencing the thermal regime. Further detailed geophysical surveys, potentially including deeper seismic profiling and gravimetric or magnetotelluric studies, could provide critical data to guide the exploration of boreholes, geothermal gradient wells and further surface temperature measurements. Gamma-spectrometer measurements can offer valuable insights into the water's radioactivity and its potential heating through radioactive decay, and laboratory measurements of geoelectrical

properties on rock samples from boreholes or outcrops can also be beneficial. These efforts would not only advance our geological understanding but could also lay the groundwork for sustainable geothermal development, contributing to regional energy security. Additionally, this research supports the potential establishment of health and wellness centers that leverage the unique thermal properties of the *Aguas de Vichy* springs, which could foster new opportunities for regional development through tourism.

Conclusion

The integration of synthetic modeling with ERT data from transects 1, 2, and 4 enabled the identification of a geothermal fluid plume characterized by resistivities below $10 \, \Omega \cdot m$. This anomaly is interpreted as a thermal saline fluid migrating laterally from the vicinity of the fault zone into the hosting aquifer and to the thermal springs. The plume displays a lateral dispersion pattern, gradually attenuating towards the southeast, and becomes untraceable in ERT 3, suggesting a loss of thermal signature or reduced connectivity beyond that point. The lithological heterogeneity of the aquifer is consistent with this irregular dispersal. Furthermore, induced polarization (IP) measurements along ERT 2 and ERT 3 revealed chargeability anomalies associated with clay-rich layers, located both within the aquifer matrix and near its upper boundary. These findings suggest the presence of local confining units that may influence the flow and accumulation of geothermal fluids by restricting vertical permeability and enhancing heat retention in certain zones.

The inclusion of TDEM soundings provided crucial depth extension beyond the resolution of ERT. TDEM-1 revealed a deep conductive anomaly that can be interpreted as a geothermal reservoir, reinforcing the potential role of the main fault in vertical fluid migration. TDEM-2, acquired alongside ERT 4, highlighted a deeper low-resistivity layer beneath a transitional resistive horizon, suggesting possible hydraulic connectivity with the reservoir at depth.

Overall, our research points to a complex geothermal system strongly influenced by local geological and structural conditions, particularly the fault systems that appear to enhance fluid circulation and thermal convection. The observed geothermal plume aligned with the fault trace, combined with the deep low-resistivity anomalies identified in TDEM-1 and TDEM-2, is consistent with the presence of upward migration of thermal fluids from depth. These results indicate that the system may not be governed solely by deep advective flow, as previously proposed (Alfaro,

2017), but may also involve buoyancy-driven convection across major faults. While previous geochemical studies have proposed a saline deep infiltration as the origin of the fluids (Alfaro and Ortiz, 2011), our findings complement this hypothesis by providing geophysical imaging of a vertical thermal input, pointing to a more dynamic and vertically connected geothermal regime. Finally, this study highlights the need for further exploration and in-depth analysis of the Aguas de Vichy geothermal system, as well as other potential sites in Santander and across Colombia. Such efforts will be essential for assessing the true extent of geothermal resources and for their potential integration into the nation's broader energy strategy, supporting Colombia's transition towards a more sustainable and diversified energy future.

Declaration of Generative AI and AI-Assisted Technologies

During the preparation of this work, the author(s) used ChatGPT (OpenAI) to assist with language editing, text structuring, and clarity improvements. After using this tool, the author(s) thoroughly reviewed and edited the content as needed and take full responsibility for the content of the published article.

References

Abd Malik, A. K., Madun, A., Dan, M. F. M., Tajudin, S. A. A., Talib, M. K. A., Azmi, M. I. S., Noh, K. A. M., and Joret, A. (2022). The effect of particle size towards resistivity and chargeability for groundwater interpretation. In *IOP Conference Series: Earth and Environmental Science*, volume 1003, page 012031. IOP Publishing.

Akhtar, N., Mislan, M., Syakir, M., Anees, M. T., and Yusuff, M. (2021). Characterization of aquifer system using electrical resistivity tomography (ert) and induced polarisation (ip) techniques. In *IOP Conference Series: Earth and Environmental Science*, volume 880, page 012025. IOP Publishing.

Alfaro, C. (2017). Geotermia en colombia: Proyecciones y plan de trabajo del servicio geológico colombiano. In *Reunión Nacional de Geotermia (RENAG) on Dic 5, 2017, Manizales, Colombia*.

Alfaro, C. M. and Ortiz, I. D. (2011). Inventario nacional de manantiales termales fase 2010, departamento de boyaca, santander y norte de santander. Technical report, Instituto Colombiano

de Geología y Minería (INGEOMINAS).

Alfaro, C. M., Rueda Gutiérrez, J. B., Casallas, Y. P., Rodríguez, G. Z., and Malo, J. E. (2020). Estimación preliminar del potencial geotérmico de colombia. Technical report, Servicio Geológico Colombiano, Bogotá.

Alfaro, E., Vargas, C. A., and Gutiérrez, J. (2009). Mapa preliminar de gradientes geotérmicos de colombia. Technical report, Servicio Geológico Colombiano. Accessed: 2025-09-12.

Arnason, K., Karlsdottir, R., Eysteinsson, H., Flóvenz, Ó., and Gudlaugsson, S. T. (2000). The resistivity structure of high-temperature geothermal systems in Iceland. In *Proceedings of the World Geothermal Congress 2000, Kyushu-Tohoku, Japan*, pages 923–928.

Auken, E., Christiansen, A. V., Kirkegaard, C., Fiandaca, G., Schamper, C., Behroozmand, A. A., Binley, A., Nielsen, E., Effersø, F., Christensen, N. B., et al. (2015). An overview of a highly versatile forward and stable inverse algorithm for airborne, ground-based and borehole electromagnetic and electric data. *Exploration Geophysics*, 46(3):223–235.

Bona, P. and Coviello, M. (2016). Valoración y gobernanza de los proyectos geotérmicos en américa del sur: una propuesta metodológica. Technical report, Naciones Unidas Comisión Económica para América Latina y el Caribe (CEPAL).

Bu, X., Ma, W., and Li, H. (2012). Geothermal energy production utilizing abandoned oil and gas wells. *Renewable Energy*, 41:80–85.

Chabaane, A., Redhaounia, B., and Gabtni, H. (2017). Combined application of vertical electrical sounding and 2d electrical resistivity imaging for geothermal groundwater characterization: Hammam sayala hot spring case study (NW tunisia). *Journal of African Earth Sciences*, 134:292–298.

Chandrasekharam, D. and Bundschuh, J. (2008). *Low-enthalpy geothermal resources for power generation*. CRC press.

Christiansen, R., Mebrahtu, T. K., Aguil, N., and Wohnlich, S. (2024). Numerical modelling of an advective geothermal system in the central andes: Sustainable utilization through borehole heat exchangers. *Renewable Energy*, 223:119989.

Dahlin, T. and Zhou, B. (2004). A numerical comparison of 2d resistivity imaging with 10 electrode arrays. *Geophysical prospecting*, 52(5):379–398.

Dahlin, T. and Zhou, B. (2006). Multiple-gradient array measurements for multichannel 2d resistivity imaging. *Near Surface Geophysics*, 4(2):113–123.

El Nuevo Oriente (2024). Proyecto de energía geotérmica licenciado a parex se desarrollaba como plan piloto desde hace 3 años. https://elnuevoooriente.com/proyecto-de-energia-geotermica-licenciado-a-parex-se-desarrollaba-como-plan-piloto-desde-hace-3-anos. Accedido el 30 de julio de 2025.

Farina, B., Poletto, F., Mendrinos, D., Carcione, J. M., and Karytsas, C. (2019). Seismic properties in conductive and convective hot and super-hot geothermal systems. *Geothermics*, 82:16–33.

García-Arias, S., Patiño, F. A. V., Gómez, J. D. S., and Ardila, M. T. U. (2024). Mapas predictivos con redes neuronales a partir de propiedades físicas de las rocas: caso de estudio en la mesa de los santos (santander). *Revista EIA*, 21(41):4112–pp.

Gawell, K., Reed, M., and Wright, P. M. (1999). Preliminary report: Geothermal energy, the potential for clean power from the earth. *Washington, DC: Geothermal Energy Association*.

González-Idárraga, C. E. (2020). Caracterización resistiva 3d del área geotérmica de paipa, colombia. *Boletín de Geología*, 42(3):81–97.

Hermans, T., Vandenbohede, A., Lebbe, L., and Nguyen, F. (2012). A shallow geothermal experiment in a sandy aquifer monitored using electric resistivity tomography. geophysics 77: B11–b21.

Hochstein, M., Zheng, K., Pasvanoglu, S., and Vivian-Neal, P. (2013). Advective (heat sweep) geothermal systems. In *Proceedings 38th workshop on geothermal reservoir engineering, Stanford University*.

Hunt, T. M., Bromley, C. J., Risk, G. F., Sherburn, S., and Soengkono, S. (2009). Geophysical investigations of the wairakei field. *Geothermics*, 38(1):85–97.

International Geothermal Association (IGA) (2014). Best practices guide for geothermal exploration. *IGA Service GmbH Technical Report*. Available from: https://www.geothermal-energy.org.

Jorquera, C. (2021). Inaugurada primera planta de energía geotérmica en colombia. Retrieved from https://www.piensageotermia.com/inaugurada-primera-planta-de-energia-geotermica-en-colombia/.

Kana, J. D., Djongyang, N., Raïdandi, D., Nouck, P. N., and Dadjé, A. (2015). A review of geophysical methods for geothermal exploration. *Renewable and Sustainable Energy Reviews*, 44:87–95.

Llera, F. J., Sato, M., Nakatsuka, K., and Yokoyama, H. (1990). Temperature dependence of the electrical resistivity of water-saturated rocks. *Geophysics*, 55(5):576–585.

Loke, M. H. (2010). Res2dinv ver. 3.59 for windows xp/vista/7.

López-Ramos, E., Gonzalez-Penagos, F., Patiño, C. A., and López, A. (2022). Low-medium enthalpy geothermal resource assessment in deep reservoirs of the llanos basin-colombia. *CT&F-Ciencia, Tecnología y Futuro*, 12(1):13–44.

McCarter, W. (1984). The electrical resistivity characteristics of compacted clays. *Geotechnique*, 34(2):263–267.

McInnis, D., Silliman, S., Boukari, M., Yalo, N., Orou-Pete, S., Fertenbaugh, C., Sarre, K., and Fayomi, H. (2013). Combined application of electrical resistivity and shallow groundwater sampling to assess salinity in a shallow coastal aquifer in benin, west africa. *Journal of hydrology*, 505:335–345.

Mejía-Fragoso, J. C., Florez, M. A., and Bernal-Olaya, R. (2024). Predicting the geothermal gradient in colombia: A machine learning approach. *Geothermics*, 122:103074.

Mejía, E., Rayo, L., Méndez, J., and Echeverri, J. (2014). Geothermal development in colombia. *Short Course VI on Utilization of Low-and Medium-Enthalpy Geothermal Resources and Financial Aspects of Utilization*, pages 1–7.

Miall, A. (2014). *Fluvial depositional systems*, volume 14, p. 316. Cham: Springer International Publishing.

Morales, E., Veroslavsky, G., Manganelli, A., Marmisolle, J., Pedro, A., Samaniego, L., Plenc, F., Umpiérrez, R., Ferreiro, M., and Morales, M. (2021). Potential of geothermal energy in the onshore sedimentary basins of uruguay. *Geothermics*, 95:102165.

Murcia, J. A. O. (2020). Geotermia en la región central. Convenio interadministrativo 080 de 2019. Technical report, Región Administrativa y de Planeación Especial RAP-E and Universidad Distrital Francisco José de Caldas, Bogotá, Colombia. Informe técnico del Grupo de Investigación Xué y Semillero Barión.

Pesce, A. and Miranda, F. (2003). *Catálogo de manifestaciones termales de la República Argentina. Vol. I-II Región Noroeste*. SEGEMAR, Buenos Aires.

Qin, M., Zhang, B., Yu, K., Zhang, B., Wang, Z., Zhu, G., Zhen, Z., and Sun, Z. (2025). Hydrogeochemistry and heat accumulation of a mine geothermal system controlled by extensional faults. *Energies*, 18(10):2490.

Redouane, F., Jamshed, W., Devi, S. U., Prakash, M., Nasir, N., Hammouch, Z., Eid, M. R., Nisar, K., Mahammed, A., Abdel-Aty, A., Yahia, I. S., and Eed, E. (2022). Heat flow saturate of ag/mgo-water hybrid nanofluid in heated trigonal enclosure with rotate cylindrical cavity by using galerkin finite element. *Scientific Reports*, 12.

Revil, A., Cathles Iii, L., Losh, S., and Nunn, J. (1998). Electrical conductivity in shaly sands with geophysical applications. *Journal of Geophysical Research: Solid Earth*, 103(B10):23925–23936.

Romo-Jones, J. M., Arango-Galván, C., Ruiz-Aguilar, D., Avilés-Esquivel, T., and Salas-Corrales, J. L. (2021). 3d electrical resistivity distribution in los humeros and acoculco geothermal zones, mexico. *First EAGE Workshop on Geothermal Energy in Latin America*, 2021(1):1–5.

Ríos, M., Hincapié, G., and Cardona, A. (2002). Atlas de aguas subterráneas de colombia (versión 2.0). https://miig.sgc.gov.co/Paginas/Resultados.aspx?k=12006010105002000500000000. Servicio Geológico Colombiano. Accedido el 21 de agosto de 2025.

Rücker, C., Günther, T., and Wagner, F. (2017). pygimli: An open-source library for modelling and inversion in geophysics. *Computers and Geosciences*, 109:106–123.

Saad, R., Nawawi, M. N. M., and Mohamad, E. T. (2012). Groundwater detection in alluvium using 2-d electrical resistivity tomography (ert). *Electronic Journal of Geotechnical Engineering*, 17:369–376.

Sabnavis, M. and Patangay, N. (2006). *Principles and Applications of Groundwater Geophysics*, volume 40 of *AEG Publication*. Association of Exploration Geophysicists, Hyderabad, India, 3 edition.

Salazar, S. S., Muñoz, Y., and Ospino, A. (2017). Analysis of geothermal energy as an alternative source for electricity in colombia. *Geothermal Energy*, 5(1):1–12.

Scott, S., Driesner, T., and Weis, P. (2016). The thermal structure and temporal evolution of high-enthalpy geothermal systems. *Geothermics*, 62:33–47.

Sill, W. R. and Klein, J. D. (1981). The electrical properties of clay. Open-File Report 81-1230, U.S. Geological Survey, Denver, Colorado.

Spichak, V. and Manzella, A. (2009). Electromagnetic sounding of geothermal zones. *Journal of Applied Geophysics*, 68(4):459–478.

Suryadi, A., Amir, S., et al. (2019). Electrical resistivity imaging (eri) and induced polarization (ip) survey to solve water drought problem at alor gajah, melaka, malaysia. In *IOP Conference Series: Materials Science and Engineering*, volume 532, page 012025. IOP Publishing.

Telford, W. M., Geldart, L. P., and Sheriff, R. E. (1990). *Applied Geophysics*. Cambridge University Press, Cambridge, UK, 2, revised edition.

Tian, B., Lei, X., Jiang, H., Xu, C., and Song, M. (2022). Multi-method geophysical mapping of a geothermal reservoir and buried channel in langfang, northern part of china. *Journal of Environmental and Engineering Geophysics*, 27(1):1–11.

Ward, D., Goldsmith, R., Survey., U. G., Cruz, J., Jaramillo, L., and Vargas, R. (1977). *Geología de la Plancha 121 Cerrito. Escala 1:100.000*. Ingeominas.

Yan, G., Busch, B., Egert, R., Esmaeilpour, M., Stricker, K., and Kohl, T. (2023). Transport mechanisms of hydrothermal convection in faulted tight sandstones. *Solid Earth*, 14(3):293–310.

Zohdy, A. A., Eaton, G. P., and Mabey, D. R. (1974). Application of surface geophysics to ground-water investigations.

Zongjun, G., Yonggui, L., and Yaun, G. (2014). The principle of density differences drive geothermal water to move and the short-range recharge model of geothermal water in hilly area. In *Proceedings of the Thirty-Ninth Workshop on Geothermal Reservoir Engineering PROCEEDINGS, Stanford, CA, USA*, pages 24–26.